Engineering 7 (2021) 226–237

Contents lists available at ScienceDirect

Engineering

journal homepage: www.elsevier.com/locate/eng

Research
Precision Engineering—Article

Design of Microstructure Parameters on a Small Multi-Throttle Aerostatic Guideway in Photolithography

Zhongpu Wen [a,b], Jianwei Wu [a,b,*], Kunpeng Xing [a,b], Yin Zhang [a,b], Jiean Li [a,b], Jiubin Tan [a,b]

[a] Center of Ultra-Precision Optoelectronic Instrumentation Engineering, Harbin Institute of Technology, Harbin 150001, China
[b] Key Lab of Ultra-Precision Intelligent Instrumentation (Harbin Institute of Technology), Ministry of Industry Information Technology, Harbin 150080, China

ARTICLE INFO

Article history:
Received 30 June 2019
Revised 11 September 2019
Accepted 9 October 2019
Available online 30 July 2020

Keywords:
Photolithography
Multi-throttle aerostatic guideway
Microstructure
Working point
Rotational stiffness

ABSTRACT

A compact multi-throttle aerostatic guideway is the preferred structure for high precision and acceleration motion in the variable-slit system (VS) of photolithography. The presence of microstructure, such as recesses and grooves, on the guideway working surface has been found to improve the loading performance. Nevertheless, the effects on the guideway performance of changing the microstructure on the micron level are not yet clear. The mesh adaptation method, which was proposed by the authors, is employed in this paper to quantitatively study the influences of four microstructure parameters. The effect of tuning these parameters on the loading performance is revealed. The level of impact determines the proposed design process of the parameters. The characteristic feature of the proposed design process is that the working points of carrying capacity, stiffness, and rotational stiffness are unified under two-way adjusting by means of recess parameters. According to the proposed design process and tuning method, the restriction of supply pressure is lifted to a certain extent and the mutual tradeoff among the loading performances is relieved. The experimental results show that the rotational stiffness of the designed guideway, based on the tuned parameters, reached 2.14×10^4 Nm·rad^{-1} and increased by 69.8%. In a scanning test of the applied VS on argon fluoride laser (ArF) photolithography, the average scanning acceleration reached 67.5 m·s^{-2}, meeting the design specification.

1. Introduction

Due to its advantages of high speed, high precision, and low friction, the aerostatic guideway has been widely used in many applications, such as measuring instruments, precision guidance, and chip manufacturing [1,2]. Recently, as a result of developments in overlay accuracy and production efficiency in lithography, the variable-slit system (VS), which is involved in the illumination system, requires improvement in the performance of the positioning accuracy and scanning velocity [3–11]. Installed between a series of optical lenses, the VS has the function of eliminating deformation, and ultimately determines the shape and productiveness of the illumination. Therefore, the VS is considered to serve the engineering objectives of better stability and higher speed. The compact multi-throttle aerostatic guideway is the preferred option in the supporting and guiding structure of a VS. Compared with traditional aerostatic guideways, multi-throttle guideways exhibit the advantages of higher stiffness; however, they are more complicated in structure and have stringent requirements in terms of operating conditions and surface profile error [12–14].

Nakamura and Yoshimoto [15,16] have analytically studied the multi-throttle aerostatic guideway under the hypothesis of laminar and uniform flow. Their results show that the double row orifice, which has broader grooves, improves the tilt stiffness of both the pitch and roll directions. In fact, the analytical method is suitable for the study of single parameters of the microstructure, as it locks other parameters within a narrow value range to maintain the effectiveness of the discharge coefficient. The specific influence of the microstructure on the discharge coefficient has been verified experimentally by Belforte et al. [17]. Under his investigation, the compact multi-throttle aerostatic guideway shows a wide value range in microstructure parameters, which affects the discharge coefficient and, consequently, the loading performance. Thus, the use of this kind of traditional method will lead to overestimation of the loading performance. Because of the gaps in analytical and experimental methods, a performance safety margin of about 50% is stipulated in the design of an aerostatic guideway [18,19].

* Corresponding author.
E-mail address: wujianwei@hit.edu.cn (J. Wu).

https://doi.org/10.1016/j.eng.2019.09.012

This percentage is close to the contribution of the microstructure parameters to the rotational stiffness. Therefore, traditional methods are not accurate enough to reflect the microstructure in the rotational stiffness. The finite-element analysis method, which has been gradually popularized and is now recognized, provides a possible way to actually study and design the microstructure of a multi-throttle aerostatic guideway.

Kim et al. [20] studied and put forward a near-wall treatment method on a high-Reynolds-number flow in a narrow and rapid field. Gharbi et al. [21] related the Reynolds number to the thickness of finite volume grids, and established a mesh for high-Reynolds-number flow. Eleshaky [22] and Zhang et al. [23] used computational fluid dynamics (CFD) and the method of separation of variables (MSV), respectively, to verify that the downstream pressure depression has an effect on the carrying capacity and stability. Gao et al. [24] studied the influence of orifice shape on pressure depression and turbulence intensity, and found that the corner radius performed best for flow smoothness and stability. Thus, the design of the orifice and other throttle structures is determined by characteristic dimensions and target performance [25,26]. Yadav and Sharma [27] used the finite-element method (FEM) to study the effects of tilt angle on the performance of the aerostatic thrust bearing with recesses. At present, the main issue in the research and design of the compact multi-throttle aerostatic guideway is to establish the corresponding relationship between the microstructure parameters and the loading performance. Wen et al. [28,29] put forward a mesh adaptation method to capture and refine target hexahedron grids using the finite volume method (FVM). Although the structure we studied is wider and thinner than a typical structure in this field, it was possible to use the mesh adaptation method to subdivide the mesh in the whole region, especially in the region near the microstructure, based on the y^+ distribution.

The tuning of micron-level changing microstructure parameters, according to the loading performance of the multi-throttle aerostatic guideway including carrying capacity, stiffness, and rotational stiffness, was studied using the mesh adaptation method. The level of impact on the above loading performances determines the design process of microstructure parameters, including the recess diameter, recess depth, groove width, and groove depth. In this paper, a design process is put forward for the microstructure parameters of a multi-throttle aerostatic guideway. The working points of carrying capacity and stiffness are unified under adjustments of the recess diameter and average recess depth. The working points of stiffness and rotational stiffness are unified under two-way adjustment of the gradient recess depth. The proposed design process is applied in the guideway design used in the VS of photolithography.

2. Model and method

2.1. Model establishment and solving method

The multi-throttle aerostatic guideway model used in this research is based on the VS. The VS is the core component of photolithography. As shown in Fig. 1(a), a VS is installed between the quartz rod and relay lens group in an illumination system, and functions as a significant reshaping diaphragm. As shown in Fig. 1(b), the VS is employed to eliminate deformation and to provide a variable rectangular slit in the reticle stage, according to the changing exposure region. Therefore, the diaphragm scanning accuracy of the VS directly affects the overlay accuracy of a photolithography machine. Fig. 1(c) shows the VS of 90 nm-thread ArF photolithography from the Harbin Institute of Technology (HIT), including the aerostatic guideway that was independently developed. Due to its advantages of higher motion and location accuracy under long-term high frequency and high-speed scanning, this kind of aerostatic guideway is expected to improve the productivity of photolithography. As shown in Fig. 1(d), the motor and diaphragm are assembled on both sides of the aerostatic guideway. Because of the position of the quartz rod and the scanning trajectory of the diaphragm, a cantilever is applied to connect the diaphragm of the *Y*-axis and the aerostatic guide sleeve. Therefore, the rotational stiffness of this guideway directly affects the scanning and positioning accuracy of the diaphragm.

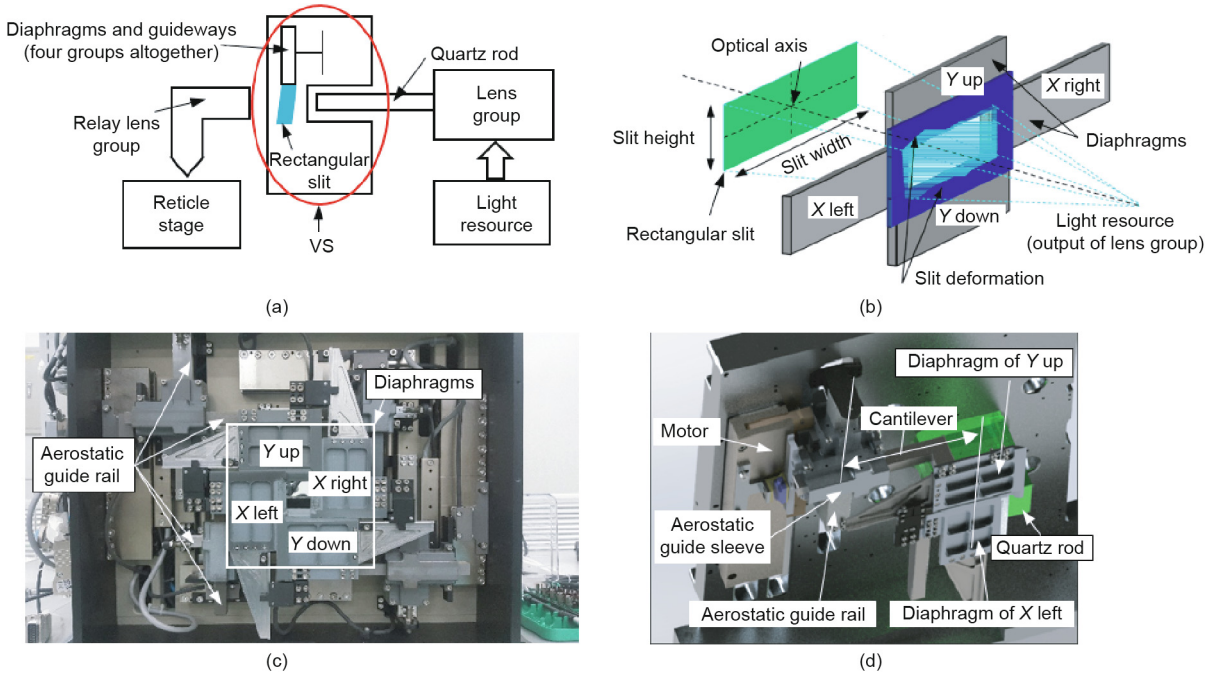

Fig. 1. VS of photolithography. (a) Placement of VS; (b) operating principle; (c) VS with aerostatic guideway; (d) cantilever of diaphragm.

Although the current aerostatic guideway has several irreplaceable advantages, continuous improvement is still needed for applied photolithography in the following three aspects: First, at least eight aerostatic guideways are restricted in a narrow space around the quartz rod. Thus, the main issue is to establish effective throttling and to provide the necessary air film stiffness, under the limitations of the throttling structure, orifice number, and distribution position. Second, the rotational stiffness provided by the aerostatic guideway should be adequate to withstand the rotational moment under high acceleration motion, which is a common and unavoidable problem of a cantilever diaphragm structure in an illumination system. Last but not least, the stability of the aerostatic guideway is restricted by the supply pressure and must submit to mutual tradeoff with other loading performances. Increasing the supply pressure will lead to a higher carrying capacity but to easier destabilization. Thus, the supply pressure should not exceed 0.4 MPa. The key to solving these problems is to design the microstructure parameters of the multi-throttle on the guideway working surface.

As shown in Fig. 2, the multi-throttle aerostatic guideway contains recesses and grooves near the orifices. When injected with high-pressure air P_0 (supply pressure), the orifice functions as a Laval nozzle and leads to the first-time throttling. The orifices reduce the pressure to P_d. Then, the recesses and grooves lead to further throttling and form a narrow air film between the guide rail and the sleeve. To study the influence of these recesses and grooves on guideway performance, the absolutely symmetric structure of the first designed guideway, labeled G_0, was improved by changing the microstructure. As shown in Table 1, structure G_0 was then experimentally improved into structures of G_1, G_2, and G_3 via non-equivalence orifice spacing, a non-equivalence recess diameter, and adding grooves, respectively.

The mesh adaptation modeling method [28,29] was employed to calculate the narrow and compact flow field generated by the multi-throttle aerostatic guideway, above. In our study, the depth of the microstructure is 10^3 smaller than the dimensions of the working surface [30]. Although small, this microstructure depth interacts well with the magnitude of the air film thickness, and then dominates the throttle area. By changing the pressure distribution, the microstructure eventually has an effect on the carrying capacity W, stiffness K_h, and rotational stiffness K_θ. Thus, the computational domain is considered to consist of a region of narrow clearance and the microstructure, which complicate the flow. Because of high speed and wall slip, the mesh near the boundary of the microstructure must be stratified for further turbulent operation. According to the principle that the first interior node of the mesh must be placed at the viscous boundary layer, the actual thickness y of the grids were predesigned. The depth of the microstructure dominates the layer number and is incorporated into the fluid calculation as well. First, the dimensionless thickness y^+ and the velocity u^+ are defined as shown Eq. (1):

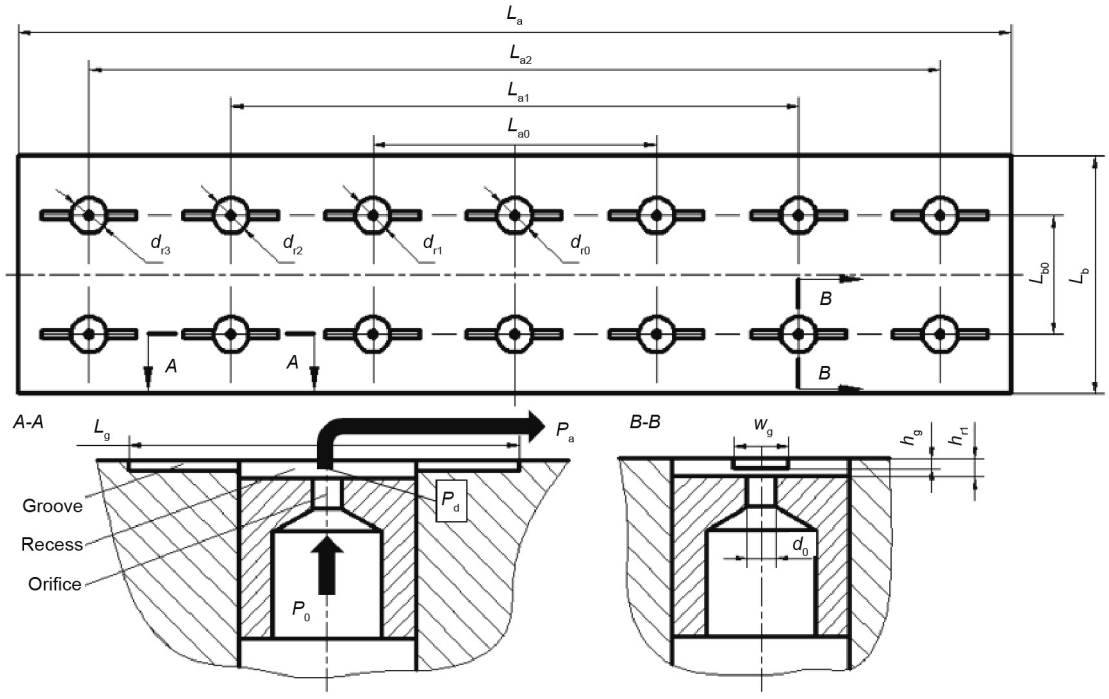

Fig. 2. A diagrammatic sketch of the multi-throttle aerostatic guideway surface. P_a: atmospheric pressure. d_0: diameter of orifice; d_{ri}: diameter of recess; h_g: depth of groove; h_{ri}: depth of recess; L_a, L_{ai}: Length of guide sleeve, spacing between orifices; L_g: length of groove; w_g: width of groove.

Table 1
Dimensions of the designed aerostatic guideway.

Structure	$L_a \times L_b$ (mm^2)	d_0 (mm)	h_{ri} (μm)	N	L_{a0} (mm)	L_{a1} (mm)	L_{a2} (mm)	d_{r0} (mm)	d_{r1} (mm)	d_{r2} (mm)	d_{r3} (mm)	$h_g \times w_g \times L_g$ (mm)
G_0	84 × 20	0.2	40	14	22	44	66	2	2	2	2	–
G_1	84 × 20	0.2	40	14	24	50	70	2	2	2	2	–
G_2	84 × 20	0.2	40	10	36	70	–	2	2.4	2.8	–	–
G_3	84 × 20	0.2	40	10	36	70	–	2	2	2	–	0.02 × 0.8 × 6

N: number of orifices.

$$u^+ = \frac{u}{u_\tau}, y^+ = \frac{u_\tau}{\mu} y \tag{1}$$

where u is the true velocity, μ is the molecular viscosity, y is the true thickness of grids; the wall shear rate, wall shear stress, and coefficient of friction are, respectively: $u_\tau = \sqrt{\frac{\tau_w}{\rho}}$, $\tau_w = C_f \times \frac{1}{2}\rho u^2$, $C_f = 0.058Re^{-1/5}$, Re is Reynolds number, and ρ is the air density.

Secondly, the actual minimum thickness of the original mesh can be expressed as y_{min}, as shown in Eq. (2):

$$y_{min} = y^+_{min}\mu/\rho u\sqrt{\frac{0.058Re^{-\frac{1}{5}}}{2}} \tag{2}$$

Next, the original mesh is analyzed to calculate the flow characteristics, such as local velocity and pressure. As shown in Eq. (3), the dimensionless velocity u^+ is modified as a mixed function of the linear wall law, which is associated with laminar flow, and of the logarithmic law, which is associated with turbulent flow. New u^+ are transformed by Eq. (1) to u for further compressible flow calculation. The above three steps are repeated to satisfy the conditions of $y^+ < 5$ at the viscous bottom layer and $y^+ < 60$ at the logarithmic layer, u^+_{lam} is the dimensionless velocity by laminar flow, and u^+_{turb} is calculated by logarithmic flow.

$$u^+ = e^{\Gamma}u^+_{lam} + e^{1/\Gamma}u^+_{turb} \tag{3}$$

$$\text{where } \Gamma = \frac{C_a(y^+)^4}{1 + C_b y^+} \text{ and } C_a = 0.01,\ C_b = 5.$$

In FVM, three-dimensional (3D) and compressible flow is being solved for turbulence. The indicial notation form in the Cartesian coordinates is given by the following:

$$\frac{\partial(\rho u_i)}{\partial x_i} = 0 \tag{4a}$$

$$\frac{\partial(\rho u_i u_j)}{\partial x_j} = -\frac{\partial P}{\partial x_i} + \frac{\partial}{\partial x_j}\left[\mu\left(\frac{\partial u_i}{\partial x_j} + \frac{\partial u_j}{\partial x_i} - \frac{2}{3}\delta_{ij}\frac{\partial u}{\partial x}\right)\right] - \partial\left(\frac{\rho\overline{u'_i u'_j}}{\partial x_j}\right) \tag{4b}$$

$$\begin{aligned}&\frac{\partial}{\partial x_j}\left\{u_j\left[C_p\frac{p}{\Re} + \frac{\rho}{2}(u_1^2 + u_2^2 + u_3^2)\right]\right\}\\ &= -\frac{\partial}{\partial x_j}\left[\left(\kappa + \frac{C_p\mu_t}{0.85}\right)\frac{\partial T}{\partial x_j} + u_i(\mu + \mu_t)\left(\frac{\partial u_i}{\partial x_j} + \frac{\partial u_j}{\partial x_i} - \frac{2}{3}\delta_{ij}\frac{\partial u}{\partial x}\right)\right]\end{aligned} \tag{4c}$$

where $\rho\overline{u'_i u'_j} = \frac{2}{3}\left(\rho k + \mu_t\frac{\partial u_i}{\partial x_i}\right)\delta_{ij} - \mu_t\left(\frac{\partial u_i}{\partial x_j} + \frac{\partial u_j}{\partial x_i}\right)$, with i = 1, 2, 3 and j = 1, 2, 3, represents the properties in three directions, respectively, and δ_{ij} is the Kronecker delta symbol, μ_t is the turbulent eddy viscosity, and μ is calculated using Sutherland's law, p is the pressure at clearance, κ is thermal conductivity and C_p is constant pressure specific heat.

The turbulent eddy viscosity is computed according to Eq. (5), and C_μ is a coefficient in k-ε model. The transport equations modeled for k (turbulent kinetic energy) and ε (dissipation rate of k) in the realizable k-ε model are shown in Eq. (6), where S is the modulus of the mean rate-of-strain tensor defined as $S = \sqrt{2S_{ij}S_{ij}}$ and a_c is the speed of sound. The constants in these equations have been established to ensure that the model performs well for certain coupled flows [31–33].

$$\mu_t = \rho C_\mu \frac{k^2}{\varepsilon} \tag{5}$$

$$\frac{\partial}{\partial t}(\rho k) + \frac{\partial}{\partial x_j}(\rho k u_j) = \frac{\partial}{\partial x_j}\left[(\mu + \mu_t)\frac{\partial k}{\partial x_j}\right] + \mu_t S^2 - \rho\varepsilon\left(1 + \frac{2k}{a_c{}^2}\right) \tag{6a}$$

$$\begin{aligned}\frac{\partial}{\partial t}(\rho\varepsilon) + \frac{\partial}{\partial x_j}(\rho\varepsilon u_j) = &\frac{\partial}{\partial x_j}\left[\left(\mu + \frac{\mu_t}{1.2}\right)\frac{\partial\varepsilon}{\partial x_j}\right] + 0.43\rho S\varepsilon\\ &- 1.9\rho\frac{\varepsilon^2}{k + \sqrt{\mu\varepsilon}}\end{aligned} \tag{6b}$$

At last, the carrying capacity W and the tilt moment M_t of the air film can be found by summing the finite element on the working face s_{sur} (surface area of each grid). The stiffness K_h is the differential of W in the direction of air film thickness Δ, and the rotational stiffness K_θ is the differential of M_t on the tilt angle θ. L_d is the arm of force in numerical calculation.

$$W = \sum(s_{sur} \cdot p) - P_a(L_a \times L_b) \tag{7}$$

$$M_t = L_d \cdot \sum(s_{sur} \cdot p) \tag{8}$$

$$K_h = \frac{\partial W}{\partial \Delta} \tag{9}$$

$$K_\theta = \frac{\partial M_t}{\partial \theta} \tag{10}$$

2.2. Steps of the research and design processes

Using the aforementioned modeling methods of mesh adaptation, we continued to study the influence of the microstructure parameters. This paper mainly examines the effects of microstructure on the loading performance. In previous studies [22–26], the influences of macrostructure parameters and conditions related to throttling have been widely researched. For example, W increases linearly in relation to P_0 and exponentially in relation to decreasing Δ. Nevertheless, these regulations do not function well on the compact aerostatic guideway of the VS, due to the size limitation and the mutual tradeoff between the carrying capacity and air film stability. Therefore, the microstructure of recesses and grooves is expected to improve the loading performance, especially for rotational stiffness, under the condition of a moderate P_0 at 0.4 MPa.

Fig. 3 shows the design processes and the corresponding solutions. First, the macrostructure is defined under the target of pressure homogenization. Then, the air film working point Δ_w, the recess diameter, the recess depth, and the grooves are researched and designed accordingly. The order is determined by the respective degree of influence of each parameter on the throttling contribution and loading performance. The recesses depth is the main research focus of this study. The ultimate objective is to improve the rotational stiffness and meet the acceleration requirement of the VS.

3. Analysis and results

3.1. Definition of macrostructure parameters and conditions

With the limits of P_0 = 0.4 MPa and Δ = 9 μm, three structures G_1, G_2, and G_3 are modeled by mesh adaptation and solved by FVM. The pressure distribution of half of the working surface is shown in Fig. 4, indicating that these structures meet the principle of pressure homogenization and the requirement of air film stability. To quantitatively study the microstructure parameters that may affect the loading performance, an appropriate macrostructure is needed first to control the variables. As shown in Table 2, CFD results of the carrying capacity, stiffness, and rotational stiffness are compared. G_1 has the simplest microstructures and retains the biggest spacing of growth for K_θ. Thus, G_1 is selected as the infrastructure for further microstructure research and design.

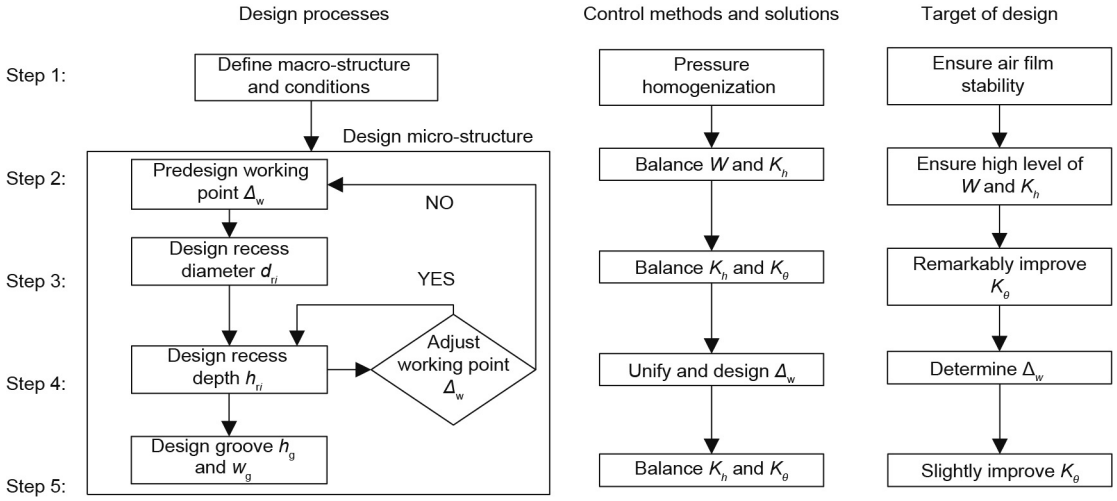

Fig. 3. Processes of research and parameter design.

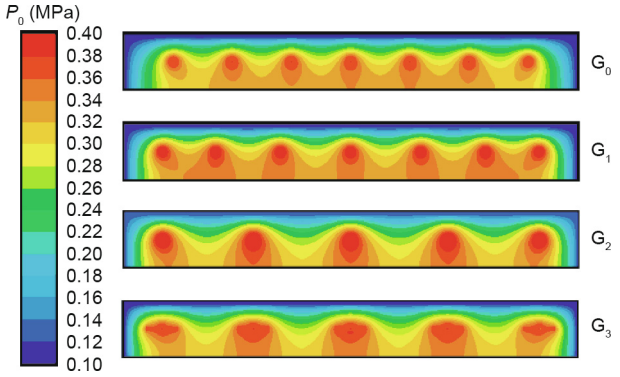

Fig. 4. Pressure distribution of structures G_0, G_1, G_2, and G_3.

Table 2
Guideway loading performances of structures G_0, G_1, G_2, and G_3.

Structure	Carrying capacity W (N)	Stiffness K_h ($N{\cdot}\mu m^{-1}$)	Rotational stiffness K_θ ($\times 10^3$ $Nm{\cdot}rad^{-1}$)
G_0	287.5	11.3	10.6
G_1	301.2	12.2	12.6
G_2	269.3	13.7	14.4
G_3	264.4	12.4	15.1

3.2. Predesign the working point Δ_w of the air film thickness

According to the adaptive method for calculating the unilateral air film's performances, the carrying capacity W and stiffness K_h of the guideway are obtained. In fact, the effective working surface of the guideway is a pair of unilateral air films positioned face to face. The average of the thickness of the two air films is the working point, as $\Delta_w = (\Delta_{down} + \Delta_{up})/2$. The working performances are the differences between the performances of the two unilateral air films, as $W = W_{down} - W_{up}$, $K_h = K_{h\text{-down}} - K_{h\text{-up}}$, and $K_\theta = K_{\theta\text{-down}} - K_{\theta\text{-up}}$. Assuming that the other macrostructures and microstructures of the working surface have been determined, the variable factor of the working point Δ_w should be defined in priority. In addition, the microstructure optimization described in the following section requires a predesigned Δ_w as well. Therefore, we determine the curves of W and K_h versus Δ_e when Δ_w varies from 4 to 14 μm. As shown in Fig. 5, the independent variable Δ_e is the working eccentricity, defined as $\Delta_e = \Delta_w - \Delta_{down} = \Delta_{up} - \Delta_w$. The minimum of Δ_{down} is set to 1 μm to avoid contact friction.

$\Delta_e = 0$ at the no-load state and Δ_e increases when loading. As shown in Fig. 5(a), the carrying capacity W of the guideway has a significantly positive correlation with Δ_e. The maximum of Δ_e is restricted by Δ_w. Thus, W has a positive correlation with Δ_w as well. Contrasting all the curves at a certain Δ_e, W increases in relation to Δ_w. Therefore, does this mean that as long as the working point increases, a larger carrying capacity will surely result? The answer is: absolutely not.

According to the $\Delta_w = 14$ μm curve shown in Fig. 5(a), W will no longer increase when the Δ_w is close to the maximum. Under this condition, the stability of the gas film will be easily destroyed by even a small external disturbance. In fact, such a gas film is not conducive to the stability of the guideway, because the self-adjusting force of the gas film may be insufficient to resist external destabilization. The assumption above can be verified from the K_h curves in Fig. 5(b). K_h increases along with Δ_w when $\Delta_e \leq 6$ μm, and K_h decreases along with Δ_w when $\Delta_w \geq 7$ μm. According to the $\Delta_w = 14$ μm curve shown in Fig. 5(b), K_h is extremely low when the Δ_e is close to the maximum. However, in the $\Delta_w = 9$ μm curve, K_h remains stable and higher, regardless of any reasonable Δ_e in the range. On the other side of the $\Delta_w = 9$ μm curve in Fig. 5(a), W is still adequate and acceptable in the variable range of Δ_e, although the maximum of Δ_e is limited by Δ_w. Therefore, $\Delta_w = 9$ μm (or close to 9 μm, because the influence of the microstructures on the working surface will be taken into consideration in the following study) is the most preferred working point for the guideway in this study, under the mutual tradeoff of W and K_h.

3.3. Influences of recess diameter d_{ri}

According to the operating conditions of the guideway, we take the stiffness K_h and rotational stiffness K_θ as the most important performances for contrast and study. To study the influence of the recess diameter d_{ri} on these performances, we limit the working point to $\Delta_w = 9$ μm for redesigning. By the adaptive method, we obtain the iso-surfaces of K_h and K_θ when d_{ri} varies from 0 to 4 mm with different guide sleeve width L_b, as shown in Fig. 6. As seen from the curves in Fig. 6(a), K_h increases monotonously with a decrease in the recess diameter, and saturates to a certain small value. As seen from the curves in Fig. 6(b), K_θ increases monotonously with the recess diameter d_{ri}, and saturates to a certain large value. This monotonous regularity is still applicable when L_b varies from 16 to 32 mm, because K_h and K_θ increase along with the effective loading area, which is determined by L_b. However, the

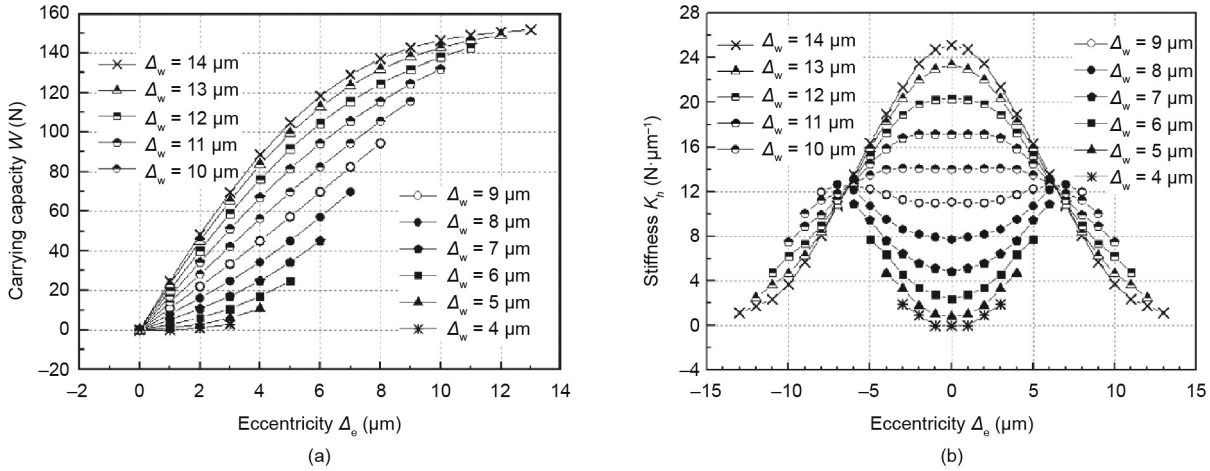

Fig. 5. The influence of Δ_e on (a) carrying capacity W and (b) stiffness K_h with different working points Δ_w.

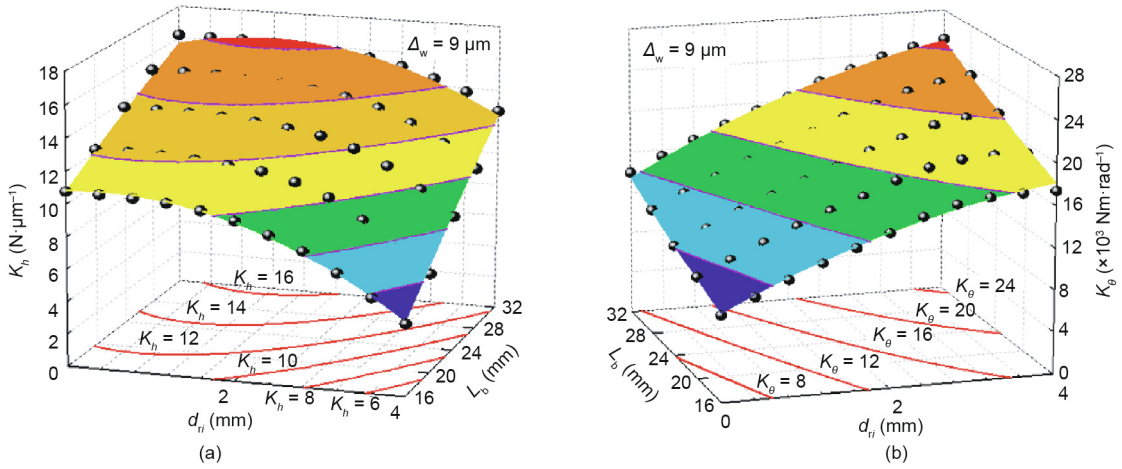

Fig. 6. The influence of d_{ri} on (a) stiffness K_h and (b) rotational stiffness K_θ with different guide sleeve widths L_b.

K_h and K_θ present a mutual tradeoff on d_{ri}, no matter how L_b changes.

A single coefficient k_{op} is employed to find a uniquely corresponding optimized d_{op} (optimization diameter of recess), under the mutual tradeoff of K_h and K_θ. The pseudo code of the optimization is given in Algorithm 1. First, the d that leads to an increase of less than 5% on K_h or K_θ is removed for filtration. Secondly, the smaller of the two suspected d_{op} is chosen by the optimization coefficient k_{op}, shown in Algorithm 1 line 18. Finally, the optimized d_{op} is employed to find the corresponding K_h and K_θ. Taking L_b = 20 mm as an example, k_{op} is assigned to meet the different operational requirements of the VS, shown in Fig. 7. Assume that the VS is operating under extreme conditions and the guideway is working at maximum acceleration. Then, the recess diameter will be optimized to d_{op} = 2.8 mm when k_{op} = 0.8 is set to meet the highest acceleration of 80 m·s^{-2}. According to the motion trajectory planning, we also have two more practical strategies, as follows: d_{op} = 2.2 mm is carried out from k_{op} = 0.6, meeting the maximum acceleration duration state when the average acceleration is 61.4 m·s^{-2}; and d_{op} = 1.4 mm is carried out from k_{op} = 0.4, meeting the minimum uniform speed distance state when the average acceleration is 49.1 m·s^{-2}. As shown in Fig. 7, the results of K_h and K_θ are found under these three different operating conditions. K_θ increases monotonously with k_{op}, because the greater the acceleration, the greater the required resistance moment and the greater the K_θ. To increase the K_θ, the K_h needs to be cut down to compensate. Thus, the optimization method can determine the optimal d_{op} and the corresponding K_h and K_θ to meet different accelerations.

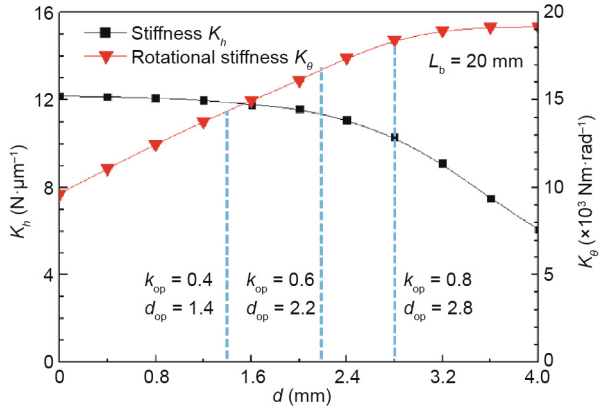

Fig. 7. The d_{op} results according to K_h and K_θ by the k_{op} optimization method when L_b = 20 mm.

Algorithm 1. Pseudo code for the optimization coefficient k_{op} method.

for all d ($0 \le d \le 4$) that have been tagged into buffer L for filtration
  establish C_h and C_θ separately
  for each remote copy of the current $K_{h(i)}$
    if $(K_{h(i)} - K_{h(i+1)})/K_{h(i)} \ge 5\%$
      pack the new stiffness with current $K_{h(i)}$
      add the corresponding d to the list of update buffer L_h
    end if
  end for
  for each remote copy of the current $K_{\theta(i)}$
    if $(K_{\theta(i+1)} - K_{\theta(i)})/K_{\theta(i)} \ge 5\%$
    pack the newly rotational stiffness with current $K_{\theta(i)}$
      add the corresponding d to the list of update buffer L_θ
    end if
  end for
  set NL = $L_h \cap L_\theta$
end for
for all d that have been tagged into buffer NL for optimization partition
  $d_{op} = \min\{k_{op} \times K_h^{-1}[(1 - k_{op}) \times K_{h(i)max}] + (1 - k_{op}) \times K_h^{-1}(K_{h(i)max}),$
  $(1 - k_{op}) \times K_\theta^{-1}[k_{op} \times K_{\theta(i)max}] + k_{op} \times K_\theta^{-1}(K_{\theta(i)max})\}$

To further verify the applicability, we optimized the recess diameter d again under different widths of the guide sleeve L_b and rows of orifices n. Clearly, a larger L_b is suitable for a bigger n, and results in an influence on the optimized results of d. Fig. 8 shows the optimized results of the dimensionless diameter $\overline{d} = nd_{op}/L_b \times 100\%$, which is the average ratio of the effective throttling length along the L_b direction, and can be used as a direct contrast. It can be seen that all the curves have the maximum point. For a certain n, a larger k_{op} will lead to a larger, conforming to the abovementioned regulation of the example of L_b = 20 mm. Furthermore, the maximum of the curves increases monotonously with k_{op}, and its growth rate slightly increases with n. For a certain k_{op}, the maximum of the curves decreases monotonously with n, and its reduction rate slightly decreases with k_{op}. According to the intersection points of these curves, we can summarize the relationship between B and n, targeted for a larger $\overline{d}$. When k_{op} = 0.6, n = 1 should be better for L_b < 20, n = 2 for 20 < L_b < 32, and n = 3 for L_b > 32. This relationship always exists when k_{op} changes.

The strategy of maximum acceleration duration is the closest to reality, in which k_{op} = 0.6. As shown in Fig. 8, the maximum dimensionless of the curves for n = 1, 2, and 3 is 20.6%, 18.7%, and 17.1%,

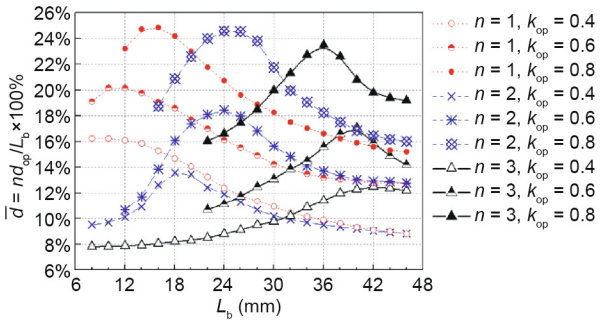

Fig. 8. The influence of L_b on optimized for different n and k_{op}.

respectively, corresponding to a guideway width L_b of 11, 24, and 39 mm. These are then transformed to a d of 2.266, 2.244, and 2.223 mm, respectively. The results show that the optimized recess diameter d_{op} = 2.2 mm in Fig. 7 is also applicable for the changing of L_b and n. Therefore, the optimization coefficient k_{op} method can be widely applied at different guide sleeve size.

3.4. Influences of recess depth h_{ri}

To study the influence of the recess depth h_{ri}, we once again take K_h and K_θ as the most important performances for contrast and study. According to the optimization results in Section 3.2, we limit the recess diameter to d_{op} = 2.2 mm. By the adaptive method, we obtain the curves of K_h and K_θ versus Δ_w with for varying recess depth h_{ri}, shown in Fig. 9. The variety regularity of K_h and K_θ on the best working points Δ_w require further research. Finally, we adjust the redesigned working point $\Delta_{w(max)}$ and confirm it by means of recess depth h_{ri} optimization.

As shown in Fig. 9(a), each curve of K_h versus Δ_w has a maximum point for a certain h_{ri}. The maximum of K_h has a significantly positive correlation with the variation of h_{ri}. The corresponding working point $\Delta_{w(max)}$ increases with h_{ri} as well. According to the current correspondence between $\Delta_{w(max)}$ and h_{ri}, the function is fitted as Eq. (11). To meet Δ_w = 9 μm, or close to this value, as was predesigned in Section 3.1, we limit the h_{ri} in a scope from 24 to 36 μm for higher K_h. This is done because a smaller or larger h_{ri} will lead to a greater deviation of $\Delta_{w(max)}$, resulting in a rapid reduction of K_h on the predesigned working point Δ_w.

$$\Delta_{w(max)} = \frac{1}{2}e^{0.08h_{ri}} + \frac{10}{3} \tag{11}$$

As shown in Fig. 9(b), each curve of K_θ versus Δ_w has a maximum point for a certain h_{ri}. The maximum of K_θ increases insignificantly along with h_{ri}, and gradually increases toward a saturation point. In addition, the corresponding working point $\Delta_{w(max)}$ remains at 11 μm and hardly changes, as it is not influenced by h_{ri}. It is clear that K_θ at Δ_w = 9 μm will be smaller than the maximum at $\Delta_{w(max)}$ = 11 μm. Thus, it is necessary to adjust $\Delta_{w(max)}$ to close to 9 μm. Furthermore, the current maximum of K_θ still holds the possibility for further improvement.

The rotational stiffness K_θ could be increased without losing stiffness K_h by means of certain special structures, while adjusting the corresponding $\Delta_{w(max)}$ to close to 9 μm. The gradient depth of the recesses is intended to realize this outcome, as shown in Fig. 10. Due to the accelerated motion, the tilt angle θ, although small, will result in a wedge-shaped air film. The film thickness varies according to the location of the recesses, rather than staying at a certain Δ_w. If the recesses were set at a unified depth, only one of the recesses would provide the maximum stiffness at its local film thickness, as shown in Fig. 10(a). This recess would be located in (or close to) the center of the guideway, and its rotating arm would be at (or close to) zero, which would provide a low rotational stiffness. As for the recesses on the right side, the stiffness would be greatly reduced, because the depth of the recesses would mismatch with the local film thickness, as can be seen from Fig. 9(a). Therefore, it is difficult to increase the rotational stiffness, although the corresponding rotating arm is big enough. This is why it is difficult to improve the rotational stiffness with recesses with a unified depth, no matter how h_{ri} changes, as can be seen from Fig. 9(b). If the recesses were set to a gradient depth, the performance would be significantly improved, as shown in Fig. 10(b). The depths of $h_{r0,1}$, h_{r2}, and h_{r3} are set to decrease in turn, in order to ensure matching to the local film thickness. Maximum stiffness is expected to be realized by following the matching rules in Fig. 9(a). The center and right recesses would then provide useful rotational stiffness for the guideways. On the

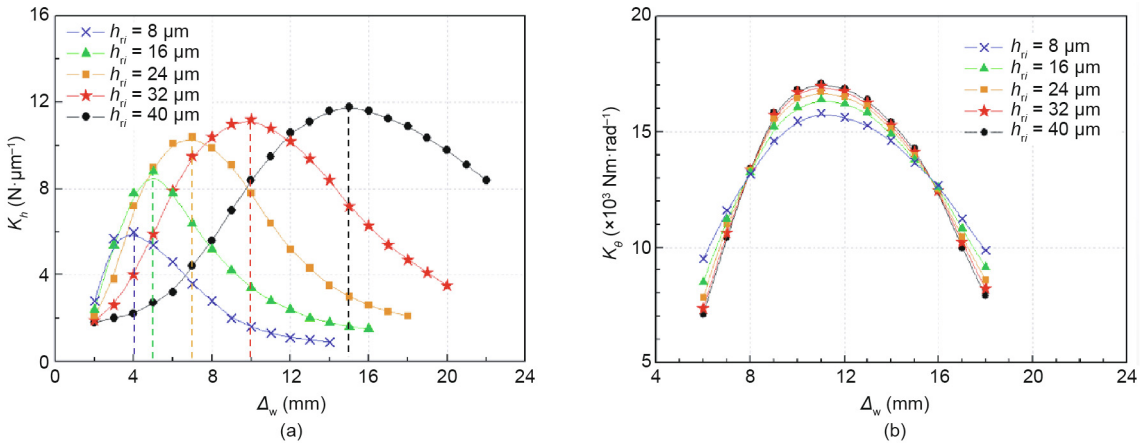

Fig. 9. The influence of Δ_w on (a) stiffness K_h and (b) rotational stiffness K_θ for different recess depths h_{ri}.

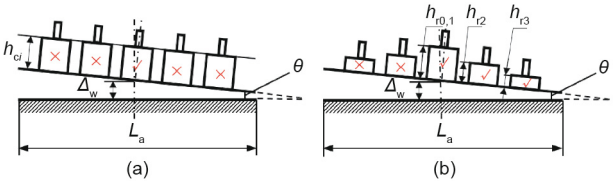

Fig. 10. A model of a wedge-shaped air film matching with the recesses of (a) unified depth and (b) gradient depth.

other side, the left recesses with a gradient depth prove to be less effective for stiffness but more effective for rotational stiffness, because of the greater depth mismatching with the local film thickness. In brief, recesses with a gradient depth will improve the stiffness on the right side, while reducing the stiffness on the left. Then, taking the rotating arm into consideration, the rotating stiffness of the guideway will be increased. The effect of the gradient depth discussed above is still valid when the tilt occurs on the left side.

To verify the deduction described above, we designed seven kinds of guideways with recesses of gradient depth, and studied their K_h and K_θ performances. As shown in Table 3, the average depth h_{avg} increases in turn from T_1 to T_7, and the depth difference ($h_{r3} - h_{r0}$) increases in a sawtooth manner. It can be seen from the curves of K_h versus Δ_w in Fig. 11(a) that the maximum of K_h has a significantly positive correlation with the variation of h_{avg}. The corresponding working point $\Delta_{w(max)}$ increases with h_{avg} as well. This variation tendency conform to the regulation of guideways with unified depth recesses. The guideways of T_5, T_6, and T_7 satisfy the scope of 24 μm ≤ h_{avg} ≤ 36 μm, while providing acceptable and adequate K_h at the predesigned Δ_w = 9 μm.

As shown in Fig. 11(b), the K_θ of the gradient depth recesses are significantly higher than those of recesses with a unified depth. More importantly, the corresponding working point $\Delta_{w(max)}$ of the maximum K_θ is changed. In the comparison of the K_θ versus Δ_w curves, the bigger the difference is in the depths of the recesses, the higher the obtained maximum of K_θ will be. The corresponding $\Delta_{w(max)}$ will also decrease more at the same time. As for the recesses with the same depth difference, such as T_2, T_3, and T_6, the maximum of K_θ increases insignificantly along with h_{avg}, conforming to the regulation of the unified depth recesses. The T_2, T_3, T_5, and T_6 guideways can significantly reduce the $\Delta_{w(max)}$, while providing acceptable and adequate K_θ at the predesigned Δ_w = 9 μm. The above results verify the deduction that the recesses' depth should match with the local film thickness for higher K_θ. Therefore, a gradient depth of the recesses can be applied to increase the rotational stiffness K_θ without losing the stiffness K_h, while adjusting Δ_w. Taking both stiffness and rotational stiffness into consideration, the T_6 guideway performs better than the others.

3.5. Influences of grooves

In a compact multi-throttle aerostatic guideway, grooves are widely applied to balance the air input. The air input is usually determined by upstream structures such as recesses and others. Therefore, it is necessary to optimize the groove parameters contrapuntally. If the previous structure is not limited, the scope of the depth of the grooves h_g and the width of the grooves w_g will change greatly with the air input. Therefore, we researched the influence of the grooves after Δ_w adjustment and recesses optimization. Based on the previous result for T_6, we further studied the influence of the h_g and w_g on K_h and K_θ.

As shown in Fig. 12(a), K_h increases monotonously with an increase in h_g, and saturates to a certain value when $h_g \geq 80$ μm generally. The saturation of K_h increases when $\Delta_w \leq 8$ μm, and decreases when $\Delta_w \geq 8$ μm. In addition, the corresponding $h_{g(max)}$ decreases with Δ_w. K_h is hardly affected by h_g when $\Delta_w \geq 12$ μm, because the increase of Δ_w leads to a larger air self-output and reduces the diversion effect of the grooves.

Table 3
Parameters of the seven guideways: T1 to T7.

Guideways	d_{op} (mm)	h_g (mm)	w_g (μm)	$h_{r0,1}$ (μm)	h_{r2} (μm)	h_{r3} (μm)	h_{avg}
T_1	2.2	1	60	24	16	8	14.4
T_2	2.2	1	60	32	16	8	16
T_3	2.2	1	60	32	24	8	19.2
T_4	2.2	1	60	32	24	16	22.4
T_5	2.2	1	60	40	24	8	24
T_6	2.2	1	60	40	24	16	27.2
T_7	2.2	1	60	40	32	24	30.4

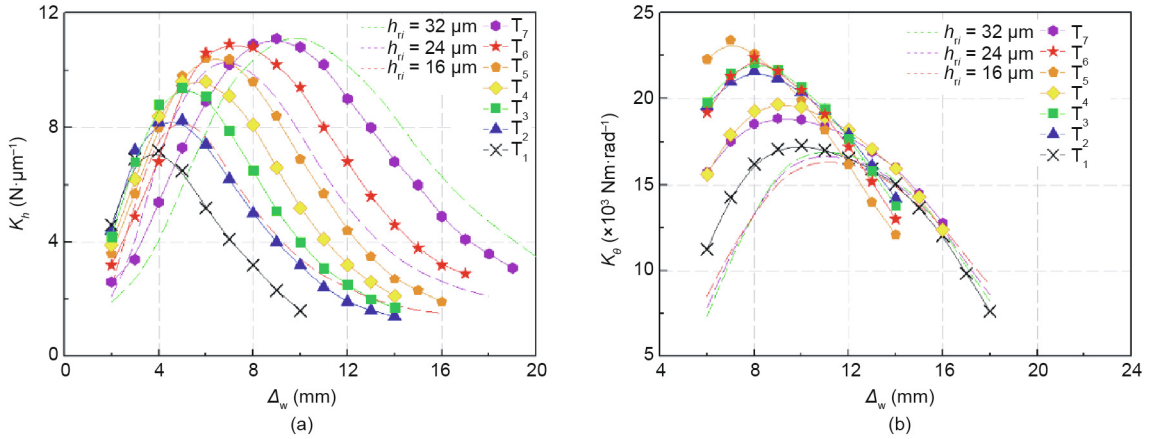

Fig. 11. The influence of Δ_w on (a) stiffness K_h and (b) rotational stiffness K_θ with gradient recess depth h_{ri}.

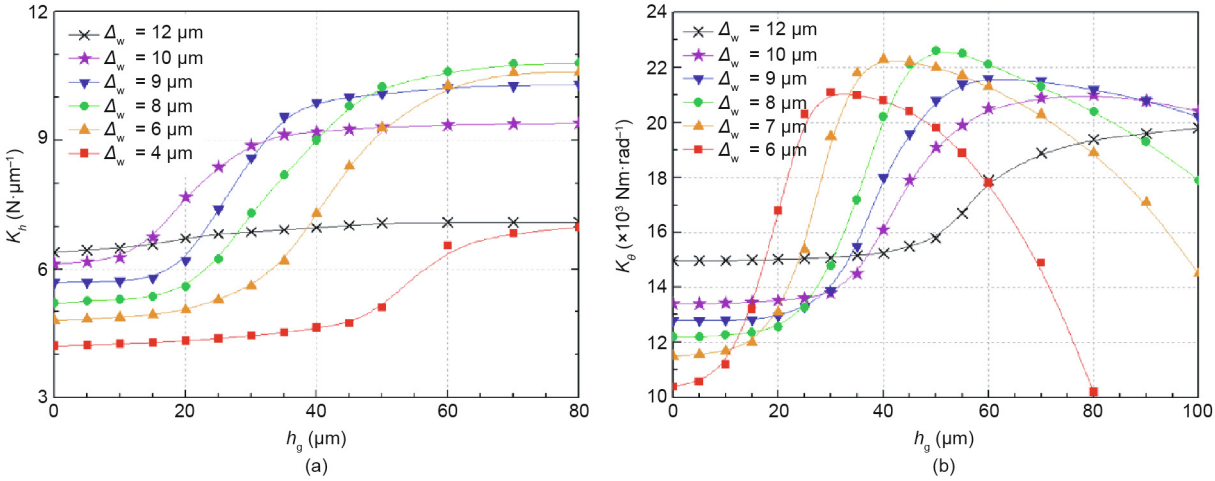

Fig. 12. The influence of h_g on (a) stiffness K_h and (b) rotational stiffness K_θ for different Δ_w.

Alternatively, the guideway itself could balance the air input, without the help of grooves. Under Δ_w = 8 μm, the saturation of K_h is the highest and the scope of $h_g \geq 50$ μm is preferred. In comparison with the predesigned Δ_w = 9 μm, the maximum of K_h is a little higher.

As shown in Fig. 12(b), each curve of K_θ versus h_g has a maximum point for a certain Δ_w. The maximum of K_θ increases when $\Delta_w \leq 8$ μm and decreases when $\Delta_w \geq 8$ μm. The corresponding $h_{g(max)}$ increases with Δ_w, as fitted by $h_{g(max)} = 12\Delta_w - 40$, according to the current correspondence. This is because a lower Δ_w results in a thinner wedge-shaped air film. Therefore, the change in h_g will be more sensitive to K_θ when $h_g \leq 70$ μm, for a low Δ_w such as the 6 μm curve. Furthermore, the maximum of K_θ occurs earlier and the corresponding $h_{g(max)}$ is smaller. In addition, a much higher h_g will result in pressure homogenization function of the grooves on a wedge-shaped air film. Therefore, a much higher h_g will lead to similar pressure and stiffness of the right and left sides, resulting in a decrease in K_θ. Under Δ_w = 8 μm, a higher K_h is obtained in the scope of $45 \leq h_g \leq 70$ μm. In comparison with the predesigned Δ_w = 9 μm, K_h is mostly higher for the same h_g scope. Considering the regulations from Figs. 12(a) and (b), a reasonable scope for h_g should be from 45 to 70 μm, based on the previous result for T_6. This is consistent with the predesigned h_g = 60 μm in Section 3.3.

As shown in Fig. 13(a), each curve of K_h versus w_g has a maximum point for a certain Δ_w. The maximum of K_h increases when $\Delta_w \leq 8$ μm and decreases when $\Delta_w \geq 8$ μm. The corresponding $w_{g(max)}$ increases with Δ_w, as fitted by $w_{g(max)} = 0.1\Delta_w + 0.2$, according to the current correspondence. This is because a lower Δ_w, such as Δ_w = 4 μm, leads to more significant effects of w_g on K_h. In contrast, a higher Δ_w, such as Δ_w = 12 μm, leads to smaller effects of w_g on K_h. In addition, K_h will decrease when w_g increases to the same magnitude as the guideway width L_b, because a wider w_g will share the effective working surface, decrease the average pressure in the air film, and finally decrease K_h.

As shown in Fig. 13(b), each curve of K_θ versus w_g has a maximum point for a certain Δ_w. The maximum of K_θ decreases along with the increases of Δ_w, and the corresponding $w_{g(max)}$ increases with Δ_w according to the current correspondence. This shows that the curves of K_θ versus w_g have similar characteristics to K_h, because the influences of w_g on K_h dominate the variation tendency of K_θ, especially for the significant influences at lower w_g. Considering the regulations from Figs. 13(a) and (b), a reasonable scope for w_g should be from 0.8 to 1 mm, based on the previous result for T_6. This is consistent with the predesigned w_g = 1 mm in Section 3.3.

According to the analysis and optimization results shown in Figs. 12 and 13, Δ_w = 8 μm performs the best in terms of K_h and K_θ in comparison the others for this specific macrostructure and microstructure. In contrast, the performance is slightly worse at Δ_w = 9 μm, which coincides with the T_6 results of K_h (Δ_w = 8 μm) > K_h (Δ_w = 9 μm), and K_θ (Δ_w = 8 μm) > K_θ (Δ_w = 9 μm) in

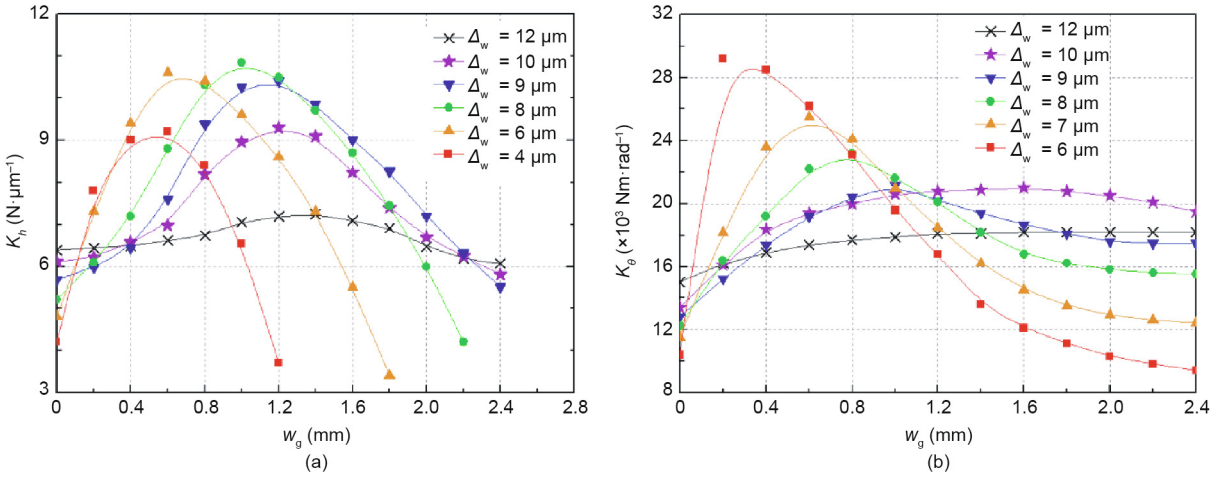

Fig. 13. The influence of w_g on (a) stiffness K_h and (b) rotational stiffness K_θ for different Δ_w.

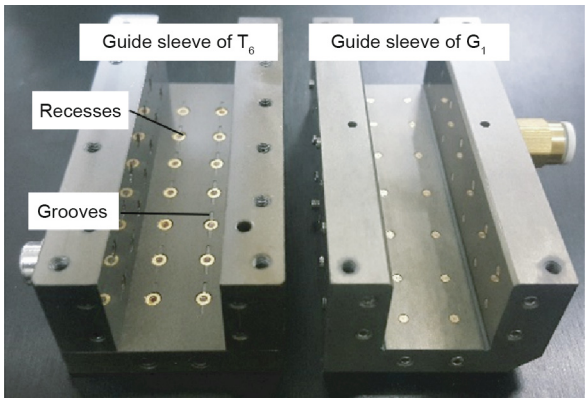

Fig. 14. C-shaped guide sleeves of the aerostatic guideways for the experiment.

Fig. 11. However, adjusting the working point to Δ_w = 8 μm is unnecessary, because Δ_w = 9 μm performs better at any eccentricity Δ_e, except for the maximum Δ_e = 7 μm shown in Fig. 5(b).

4. Experiment and verification

4.1. Experimental setup of carrying capacity W *and tilt moment* M_t

As shown in Fig. 14, the guide sleeves G_1 and T_6 are made of the aluminum alloy $AlZnMgCu_{1.5}$, with the surface having undergone anodic oxidation. The guide rail is made of the alloy steel 38CrMoAl, followed by surface nitriding.

The measurement principle of the carrying capacity W and tilt moment M_t are shown in Figs. 15(a) and (b). Unlike in the simulation, the independent variable is the load quality, which is modified at a constant step; this is accomplished by loading

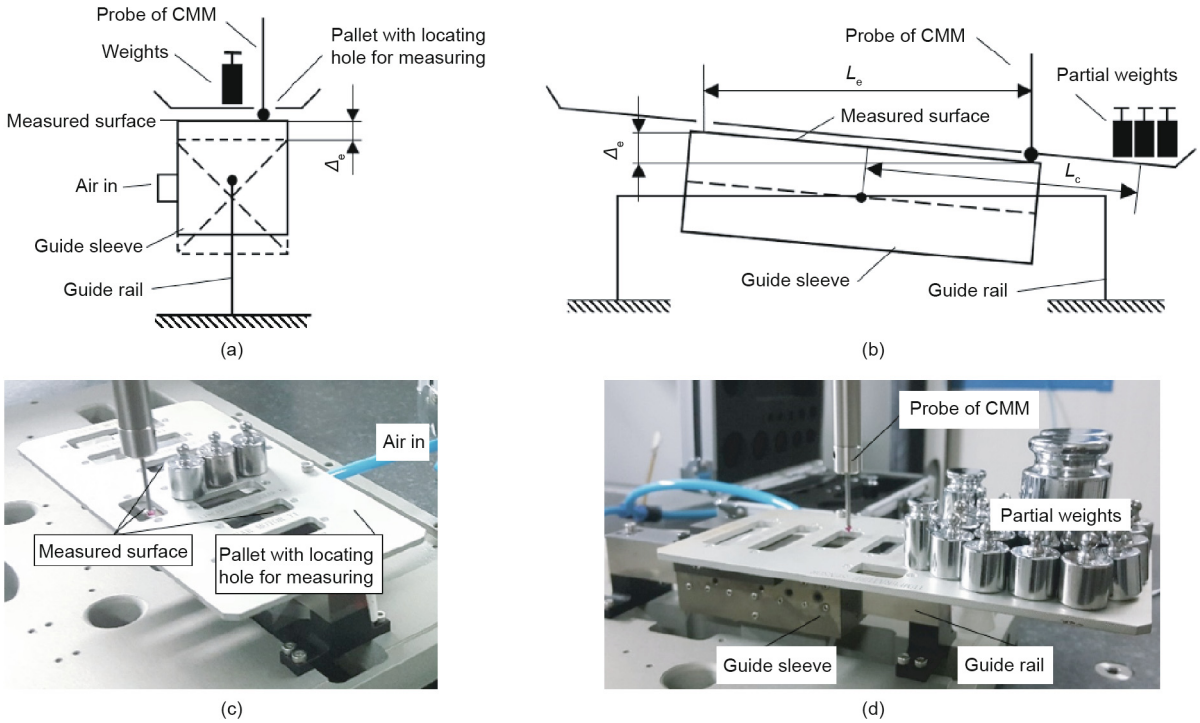

Fig. 15. Measurement principle and experimental setup. (a) Measurement for W; (b) measurement for M_t; (c) setup for W; (d) setup for M_t. CMM: coordinate measuring machine.

discrete weights onto the pallet. The tilt moment is measured by $M_t = W \cdot L_c$. L_c is the arm of force by experiment. The dependent variable is the relative altitude Δ_e, which is measured by a coordinate measuring machine (CMM) and processed by the software package QUINDOS 7. As shown in Fig. 15(c), Δ_e is equal to the surface spacing, evaluated from three or four points on the measured surface. As shown in Fig. 15(d), Δ_e is equal to the difference of the inclined surface, evaluated from two points at a distance of L_e.

4.2. Verification on stiffness, rotational stiffness, and acceleration performance

The carrying capacity W and the tilt moment M_t can be immediately measured from the setup. Then, the stiffness K_h and rotational stiffness K_θ are obtained by means of Eqs. (9) and (10). As shown in Fig. 16(a), the K_h curve of T_6 is steadier. As for the eccentricity from the weight of the sleeve and the pallet, Δ_e cannot be measured from zero. As shown in Fig. 16(b), the rotational stiffness of T_6 is improved by the design of the microstructure parameters. The result shows that $K_\theta = 2.14 \times 10^4$ Nm·rad^{-1}; this value has increased by 69.8% and aligns with the CFD result.

In the scanning test of the applied ArF photolithography, the aerostatic guideway was driven and monitored by an Elmo recorder after the design of the microstructure parameters. As shown in Fig. 17, the average scanning acceleration reached 67.5 m·s^{-2}, which meets the design specification of 61.4 m·s^{-2} mentioned in Section 3.3.

These results show that the design and tuning of microstructure parameters can improve the rotational stiffness of the guideway under the condition of a medium pressure supply, with no loss of stiffness. This practical application shows that the multi-throttle aerostatic guideway designed by the proposed method satisfies the requirement of high acceleration scanning motion in photolithography.

5. Conclusions

The following conclusions can be made:

(1) The relevance between the working point and the microstructure parameters was established using the mesh adaptation method. Furthermore, the effect of the microstructure parameters at the micron level on the loading performance of the multi-throttle aerostatic guideway was revealed. This study shows that the diameter and depth of the recess have a relatively significant influence on the rotational stiffness. In particular, the method of designing a gradient recess depth in order to tune the working point was discovered.

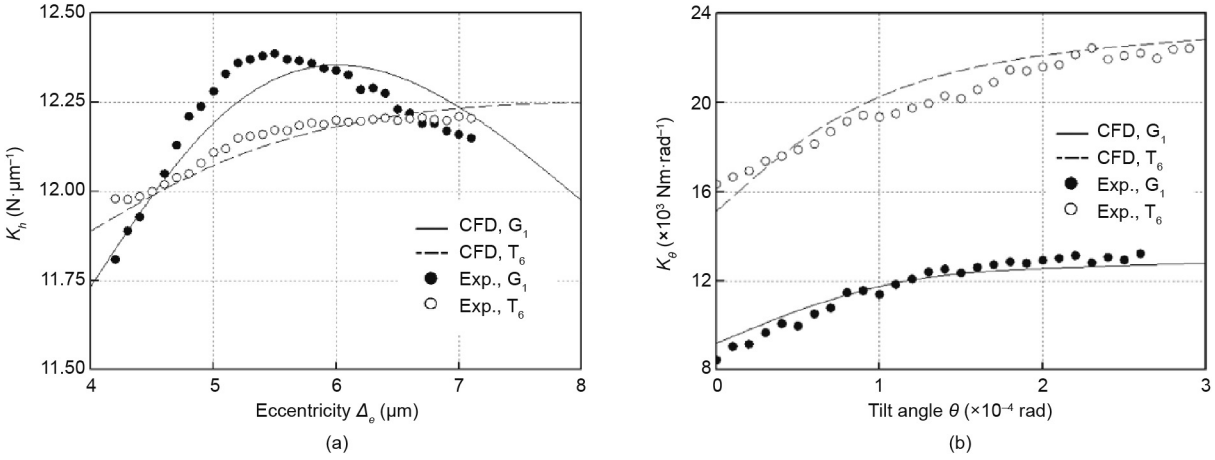

Fig. 16. CFD and experimental (Exp.) results of (a) stiffness K_h and (b) rotational stiffness K_θ of G_1 and T_6.

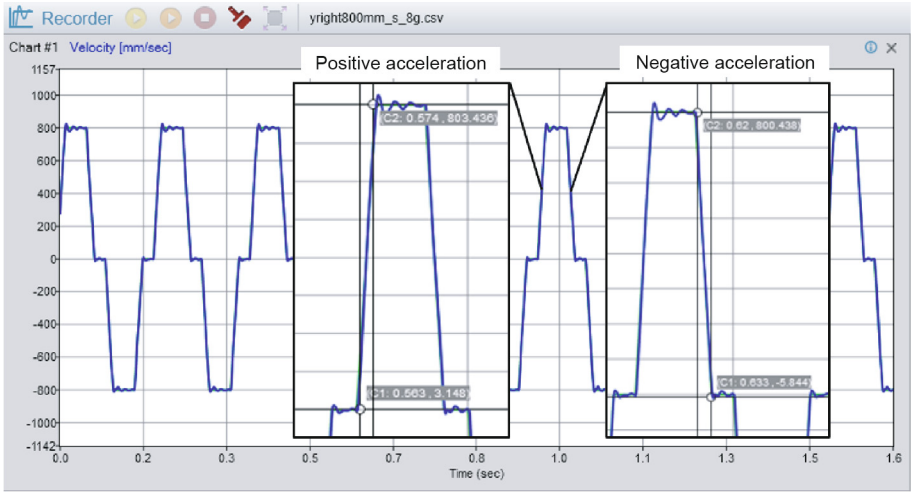

Fig. 17. Velocity monitored by an Elmo recorder in the scanning test of the applied ArF photolithography.

(2) A type of design process for the microstructure parameters of a multi-throttle aerostatic guideway was put forward, with the aim of improving the rotational stiffness. The working points of carrying capacity and stiffness were unified by tuning the recess diameter and average recess depth. The working points of stiffness and rotational stiffness were unified by two-way adjusting the gradient recess depth. To a certain extent, the design process can lift the restriction of the supply pressure and solve the mutual tradeoff among loading performances. Thus, the rotational stiffness can be effectively promoted under medium pressure by the design of the microstructure parameters.

(3) The experimental results showed an increase in rotational stiffness of 69.8% as a result of the microstructure parameters design. The alignment of the CFD and experimental results verified the effectiveness of the design process. A compact multi-throttle aerostatic guideway was applied in the VS of ArF photolithography, based on the presented microstructure parameters design process. In the scanning test, the average scanning acceleration reached 67.5 $m \cdot s^{-2}$, which meets the design specification. Furthermore, this design process for the microstructure of a multi-throttle aerostatic guideway is expected to improve the scanning performance of other components in lithography, laying the foundation for cross-generational developments in accuracy and productivity.

Acknowledgements

This work was funded by the National Natural Science Foundation of China (51675136), the National Science and Technology Major Project (2017ZX02101006-005), and the Heilongjiang Natural Science Foundation (E2017032).

Compliance with ethics guidelines

Zhongpu Wen, Jianwei Wu, Kunpeng Xing, Yin Zhang, Jiean Li, and Jiubin Tan declare that they have no conflict of interest.

References

[1] Yang P, Takamura T, Takahashi S, Takamasu K, Sato O, Osawa S, Takatsuji T. Development of high-precision micro-coordinate measuring machine: multi-probe measurement system for measuring yaw and straightness motion error of *XY* linear stage. Precis Eng 2011;35(3):424–30.
[2] Qi E, Fang Z, Sun T, Chen J, Liu C, Wang J. A method for predicting hydrostatic guide error averaging effects based on three-dimensional profile error. Tribol Int 2016;95:279–89.
[3] Levinson HJ. Principles of lithography. 3rd ed. Bellingham: Society of Photo-Optical Instrumentation Engineers; 2010.
[4] Mizoguchi H, Nakarai H, Abe T, Ohta T, Nowak KM, Kawasuji Y, et al. LPP-EUV light source development for high volume manufacturing lithography. In: Proceedings of the 2013 SPIE Advanced Lithography; 2013 Feb 24–28; San Jose, CA, USA; 2013. p. 1–11.
[5] Zhong B, Bai B, Li J, Zhang Y, Fu Y. Hierarchical tracking by reinforcement learning-based searching and coarse-to-fine verifying. IEEE Trans Image Process 2019;28(5):2331–41.
[6] Laidler D, D'havé K, Hermans J, Cheng S. Mix and match overlay optimization strategy for advanced lithography tools (193i and EUV). In: Proceedings of the 2012 SPIE Advanced Lithography; 2012 Feb 13–15; San Jose, CA, USA; 2012. p. 1–11.
[7] Lai K, Liu C, Pitera J, Dechene DJ, Schepis A, Abdallah J, et al. Computational aspects of optical lithography extension by directed self-assembly. In: Proceedings of the 2013 SPIE Advanced Lithography; 2013 Feb 24–28; San Jose, CA, USA; 2013. p. 1–13.
[8] Lin Y, Zhong B, Li G, Zhao S, Chen Z, Fan W. Localization-aware meta tracker guided with adversarial features. IEEE Access 2019;7:99441–50.
[9] Peeters R, Lok S, van Alphen E, Harned N, Kuerz P, Lowisch M, et al. ASML's NXE platform performance and volume introduction. In: Proceedings of the 2013 SPIE Advanced Lithography; 2013 Feb 24–28; San Jose, CA, USA; 2013. p. 1–8.
[10] Zhang W, Gong Y. Vector analysis of diffractive optical elements for off-axis illumination of projection lithographic system. Acta Opt Sin 2011;31(10):1005002. Chinese.
[11] Raghunathan S, Munder A, Hartley J, Sohn J, Orvek K. Correlation of overlay performance and reticle substrate non-flatness effects in EUV lithography. In: Proceedings of the 2009 SPIE Photomask Technology; 2009 Sept 14–17; Monterey, CA, USA; 2009. p. 1–9.
[12] Tanaka Y, Hara T, Kitamura H, Ishikawa T. Synchronization of picosecond laser pulses to the target X-ray pulses at SPring-8. Nucl Instrum Methods Phys Res A 2001;467–468(Pt 2):1451–4.
[13] Taghizadeh MR, Blair P, Layet B, Barton IM, Waddie AJ, Ross N. Design and fabrication of diffractive optical elements. Microelectron Eng 1997;34(3–4):219–42.
[14] Broers AN. Resolution, overlay, and field size for lithography systems. IEEE Trans Electron Devices 1981;28(11):1268–78.
[15] Nakamura T, Yoshimoto S. Static tilt characteristics of aerostatic rectangular double-pad thrust bearings with compound restrictors. Tribol Int 1996;29(2):145–52.
[16] Nakamura T, Yoshimoto S. Static tilt characteristics of aerostatic rectangular double-pad thrust bearings with double row admissions. Tribol Int 1997;30(8):605–11.
[17] Belforte G, Colombo F, Raparelli T, Trivella A, Viktorov V. Comparison between grooved and plane aerostatic thrust bearings: static performance. Meccanica 2011;46(3):547–55.
[18] Liu T, Li YT, Liu YH, et al. [Aerostatic lubrication]. Harbin: Harbin Institute of Technology Press; 1998. Chinese.
[19] Rowe WB. Hydrostatic, aerostatic and hybrid bearing design. Oxford: Butterworth-Heinemann; 2013.
[20] Kim JY, Ghajar AJ, Tang C, Foutch GL. Comparison of near-wall treatment methods for high Reynolds number backward-facing step flow. Int J Comput Fluid Dyn 2005;19(7):493–500.
[21] Gharbi EN, Absi R, Benzaoui A, Amara EH. Effect of near-wall treatment on airflow simulation. In: Proceedings of the 2009 International Conference on Computational Methods for Energy Engineering and Environment; 2009 Nov 20–22; Sousse, Tunisia; 2009.
[22] Eleshaky ME. CFD investigation of pressure depressions in aerostatic circular thrust bearings. Tribol Int 2009;42(7):1108–17.
[23] Zhang J, Zou D, Ta N, Rao Z. Numerical research of pressure depression in aerostatic thrust bearing with inherent orifice. Tribol Int 2018;123:385–96.
[24] Gao S, Cheng K, Chen S, Ding H, Fu H. CFD based investigation on influence of orifice chamber shapes for the design of aerostatic thrust bearings at ultra-high speed spindles. Tribol Int 2015;92:211–21.
[25] Aoyama T, Kakinuma Y, Kobayashi Y. Numerical and experimental analysis for the small vibration of aerostatic guideways. CIRP Ann 2006;55(1):419–22.
[26] Aoyama T, Koizumi K, Kakinuma Y, Kobayashi Y. Numerical and experimental analysis of transient state micro-bounce of aerostatic guideways caused by small pores. CIRP Ann 2009;58(1):367–70.
[27] Yadav SK, Sharma SC. Performance of hydrostatic tilted thrust pad bearings of various recess shapes operating with non-Newtonian lubricant. Finite Elem Anal Des 2014;87:43–55.
[28] Wen ZP, Wu JW, Zhang Y, Cui JW, Tan JB. Improving the rotational stiffness of compact aerostatic guideway by micro-structures optimization. IEEE Access 2019;7:55780–7.
[29] Wen ZP, Wu JW, Tan JB. An adaptive modeling method for multi-throttle aerostatic thrust bearing. Tribol Int 2020;149:105830.
[30] Geng YQ, Yan YD, Wang JQ, Brousseau E, Sun YW, Sun YZ. Fabrication of periodic nanostructures using AFM tip-based nanomachining: combining groove and material pile-up topographies. Engineering 2018;4(6):787–95.
[31] Zhou Q, Zhong B, Zhang Y, Li J, Fu Y. Deep alignment network based multi-person tracking with occlusion and motion reasoning. IEEE Trans Multimed 2019;21(5):1183–94.
[32] Kim SE, Choudhury D, Patel B. Computations of complex turbulent flows using the commercial code fluent. In: Salas MD, Hefner JN, Sakell L, editors. Modeling complex turbulent flows. Dordrecht: Kluwer Academic Publishers; 1999. p. 259–76.
[33] Zhong B, Yao H, Chen S, Ji R, Chin TJ, Wang H. Visual tracking via weakly supervised learning from multiple imperfect oracles. Pattern Recognit 2014;47(3):1395.